Correction: 31 August 2015

www.sciencemag.org/cgi/content/full/science.aac6383/DC1

Supplementary Materials for

Slip pulse and resonance of the Kathmandu basin during the 2015 Gorkha earthquake, Nepal

J. Galetzka, D. Melgar, J. F. Genrich, J. Geng, S. Owen, E. O. Lindsey, X. Xu, Y. Bock, J.-P. Avouac,* L. B. Adhikari, B. N. Upreti, B. Pratt-Sitaula, T. N. Bhattarai, B. P. Sitaula, A. Moore, K. W. Hudnut, W. Szeliga, J. Normandeau, M. Fend, M. Flouzat, L. Bollinger, P. Shrestha, B. Koirala, U. Gautam, M. Bhatterai, R. Gupta, T. Kandel, C. Timsina, S. N. Sapkota, S. Rajaure, N. Maharjan

*Corresponding author. E-mail: avouac@gps.caltech.edu

Published 6 August 2015 on *Science* Express
DOI: 10.1126/science.aac6383

This PDF file includes:

Other Supporting Online Material for this manuscript includes the following:
(available at www.sciencemag.org/cgi/content/full/science.aac6383/DC1)

Correction: In table S1, the displacement at station SNDL was reported erroneously. The correct displacement is: east, 0.047 ±0.002 m; north, –0.223 ±0.003 m; vertical, 0.003 ±0.003 m. The PDF has been corrected.

Materials and Methods

GPS processing

We processed 5-Hz continuous GPS data from six stations in Nepal (Figure 1) at distances of 60 to 230 km from the epicenter for the day of the mainshock (April 25). Final GPS satellite orbits, Earth Rotation Parameters (ERPs) and 0.2 Hz GPS satellite clocks from CODE (Center for Orbit Determination in Europe, ftp://ftp.unibe.ch/aiub/CODE/2015/) were fixed to estimate 30 s fractional-cycle biases (FCBs) with a reference network of 43 stations located over 1000 km from Nepal. We then fixed the orbits, clocks and ERPs from the network solution to enable precise point positioning with ambiguity resolution (PPP-AR)(*35*) stations to estimate epoch-wise positions, zenith troposphere delay (ZTD) parameters, receiver clocks and phase ambiguities for all seven high-rate stations. All position estimates are with respect to the International Terrestrial Reference Frame (ITRF2008) positions and are not contaminated by any displaced reference stations. No constraints between epochs are applied to the positions, while ZTDs are estimated as random walk parameters with a power density of 0.001 mm/$s^{1/2}$. All eligible ambiguities were resolved successfully and at least six ambiguities are fixed at each epoch. Solid Earth tides, ocean tide loading and pole tide are applied and antenna phase center variations are used. According to the scatter of 10 minutes of pre-event positions, the position precision (one-sigma) is about 5 mm for the horizontal and 10 mm for the vertical components for all stations.

InSAR processing

Interferometric Synthetic Aperture Radar (InSAR) data from the Japanese Aerospace Agency (JAXA) Advanced Land Observing Satellite 2 (ALOS-2) were processed using GMTSAR (*36*) and unwrapped using SNAPHU (*37*). Images were acquired over the epicentral area on February 22 and May 3 (Descending Path 48). The perpendicular baseline was 56 m; this value is sufficiently small that errors in the SRTM-1 dataset used to remove the topographic phase do not contribute significantly to the residual. The data were acquired in Wide Swath (ScanSAR) mode which enables a swath width of 350 km, but requires precise burst alignment during operation of the satellite. ScanSAR interferometry was successfully employed for the 2008 Wenchuan earthquake (*38*) using manually aligned bursts, but ALOS-2 is the first L-band satellite to acquire burst-aligned ScanSAR imagery as a standard operating mode. We processed the Level 1.1 single-look-complex (SLC) imagery for each of the five sub-swaths using GMTSAR, which includes a 5-parameter alignment of the slave image to the master based on cross-correlation, and applied a 500m Gaussian lowpass filter to improve coherence. The resulting interferograms have phase that matches at the sub-swath boundaries despite being independently processed. We unwrapped each sub-swath using SNAPHU and then combined the sub-swaths into a single image by adding a multiple of 2π to ensure matching phase at the boundaries. The final result contains a linear ramp related to orbital error, which we removed using the best-fitting plane to data outside the deforming region. Finally we subsampled the data using the quad tree technique (*39*) and a total of 2230 InSAR LOS points contributed to the joint inversion.

Kinematic slip inversion

We used the main nodal plane from the USGS W-phase moment tensor solution with a strike of 295° and dip of 11° to define the faulting surface (*6*). The assumed fault was discretized into 300 10x10 km subfaults. Elastodynamic Green's functions at the 5 Hz GPS sample rate were computed for every subfault/station pair using the frequency wavenumber integration technique of Zhu and Rivera (*40*). Since velocity data are more sensitive to rupture kinematics (23) we differentiated the GPS displacement time series to velocity and low-pass filtered them with a 4 pole Butterworth filter with corner frequency at 1 Hz. It is important to note that differentiation of the GPS data would not be effective at lower sampling rates such as 1 Hz. Joint inversion of the velocity waveforms, GPS static offsets and InSAR LOS static offsets was carried out using the multi-time window method with three-knot splines (isosceles triangles) as basis functions (Ide et al. 1996). The accelerometric record from KATNP was not included in the inversion because it has no absolute timing. The inversion is carried out using non-negative least squares and the rake is constrained to values between 45 and 135. In order to model the complexity of the subfault source time functions, we allowed slip on twenty 50% overlapping triangles with 1 s rise time. With this parametrization each subfault was allowed to slip for a total of 10 s. Spatial regularization was achieved though minimum norm smoothing; constraints were placed on the L_2 norm of the model parameter vector. Temporal smoothing on the time windows was achieved with a simple first-order forward finite difference stencil. The optimal level of spatial and temporal smoothing was determined through Akaike's Bayesian Information Criterion (*41*).

The GPS velocity waveforms and InSAR LOS and GPS static offsets were weighted equally by dividing each data set by the norm of the vector containing the observations. We assumed the NEIC reported hypocentral location and time (28.147°N 84.708°E; 2015-04-25 06:11:26.270 UTC). Maximum rupture speed was constrained through trial and error (Figure S4); we find that 3.3 km/s yields the best fit to the data (Figure S4). This does not mean that slower rupture speeds are not possible; in this case early time windows will simply have little or no slip. However, rupture at earlier times than the time it would take a rupture front propagating outward from the hypocenter at 3.3 km/s was not allowed. To avoid a possible bias in the determination of the source due to amplification by site effects, we cropped the waveform at station NAST to include only the main pulse and we down weighted the horizontal components which are most affected by site effects (Figure 4).

The stress drop from the resulting slip model was estimated by computing internal strains on the fault (*42*) assuming a half space with a rigidity of 32 GPa; this corresponds to the rigidity of the layer where most of the slip occurs.

Temporal resolution and inversion calibration

There are three important questions with regards to the inversion setup which affect our conclusions: 1) Whether the observed data can be explained by variability in other aspects of the source kinematics, 2) Whether the inversion parametrization into 20 50% overlapping splines (triangles) is adequate in discerning the potential slip-rate time functions (STFs) at the individual subfaults and 3) Whether the station geometry is adequate for assessing the characteristics of the STFs, i.e., whether STF resolution is equal on all parts of the fault model.

To investigate these questions we produced an ensemble of 25 synthetic scenario ruptures. The background slip distribution for all the synthetic models is the same. It is obtained from the inversion of just the static data (InSAR+GPS) and the result is shown in Figure S9. We then turned this static model into a kinematic one by letting rupture propagate from the hypocenter at 5 different rupture speeds, 2.8, 3.0, 3.2, 3.4 and 3.6 km/s. For each rupture speed we also used regularized Yoffe STF with a rise time of 2, 4, 6, 8 and 10s. We assumed that acceleration time to peak slip rate, τ_s is always 25% of the rise time. We have thus a total of 25 scenario events, all with the same total slip but varying in rupture speed and STF rise time. For each synthetic test case we modeled the 5 Hz velocity waveforms at the locations of the GPS stations.

Before analyzing the synthetic models further insight into the likelihood that the vertical velocity pulse at KKN4 reflects the rise time of the slip function beneath the site can be gleaned by rotating the seismograms for that site into fault parallel and fault normal directions (Figure S8). Since the station is only 13 km away from the source it is to be expected that the ground motions are dominated by intermediate field terms in the elastodynamic solution. As such, the time taken for the displacements to grow to the final static offset are directly related to the local rise time. Although the waveforms also include the contributions of surface waves, it is clear from the waveforms that the duration of the vertical velocity pulse correlates well with the static field growth.

As noted, a key assumption of this study is that the pulse observed on the vertical velocity waveform at the bedrock site KKN4 reflects a propagating slip pulse with long rise time. Figure S9 shows the predicted vertical waveforms at this station for the 25 scenario events. The comparison between the observed data (black trace) and the synthetics suggests that this assumption is reasonable. Shorter STFs should produce appreciably higher amounts of high frequency energy that are conspicuously absent in the observed data, and although the rupture speed has some effect on the synthetics it does not greatly alter the shape or duration of the main pulse.

To assess whether the temporal parametrization in the inversion is suitable, we add realistic noise to the synthetic time series for the scenario events and then invert them with the 20 triangle parametrization. We measure the standard deviation of 60 s of pre-event noise at each site and use that to add white Gaussian noise to the time series. We then invert only the synthetic velocity data (disregarding the InSAR and displacement data) in an effort to determine if we can recover the subfault STF. We perform the inversions at 6 different levels of temporal smoothness with the values of the regularization parameter logarithmically spaced between 10^{-4} and 10^{1}. An example of the along strike STFs for different levels of smoothing is shown in Figure S10. The figure shows that although recovery of the STFs is not perfect, the total duration (the rise time) of each STF is well constrained. The plot also shows no significant along-strike bias. It also shows that a temporal smoothing value of 0.01-0.1 is suitable and that the effect of over smoothing (Figure 10C) is to produce artificially long STFs. This is easily understood as due to late occurring small amplitude triangles, which are used by the inversion in an attempt to fit the noise. If the smoothing is too strong the STFs will try to encompass these artifacts and the resulting STFs are artificially long.

We further test whether the inversion parametrization is sufficient to discern between STFs of different rise times. Figure S11 shows the STFs inverted for the same along-strike profile for a rupture velocity of 3.2 km/s and a smoothing value of 0.1 for 4

models with different rise-times at 4, 6, 8 and 10 s. Again, recovery of the STFs is not perfect, but in general for the rise times tested the parametrization is sufficient to determine the rise times of the individual subfaults.

Thus, the observations at station KKN4 of the pulse in the vertical velocity waveform, and the obvious absence of high frequency strong shaking along with the synthetic tests suggest that the event indeed can be characterized by a propagating slip pulse with a long rise time. Furthermore, the sensitivity tests indicate that while the shapes of the individual STFs at each subfault are affected by noise, the total duration, or rise time, of each STF is well constrained by the available network of observing stations.

Aftershocks

The Department of Mines and Geology (DMG), Nepal, operates, in collaboration with the Departement Analyse Surveillance Environnement (DASE), France, a nationwide seismic network consisting primarily of 21 vertical component short period sensors (ZM500) (*43*). We used the seismicity catalogue of events with local magnitude M_L larger than 4.0 produced by the DMG from the mainshock on April 25 to May 19, 2015, available at www.seismonepal.gov.np. See Pandey et al. (*43*) and Rajaure et al. (*44*) for details of the network and routine location procedure.

<insert page break then Fig S1 here>

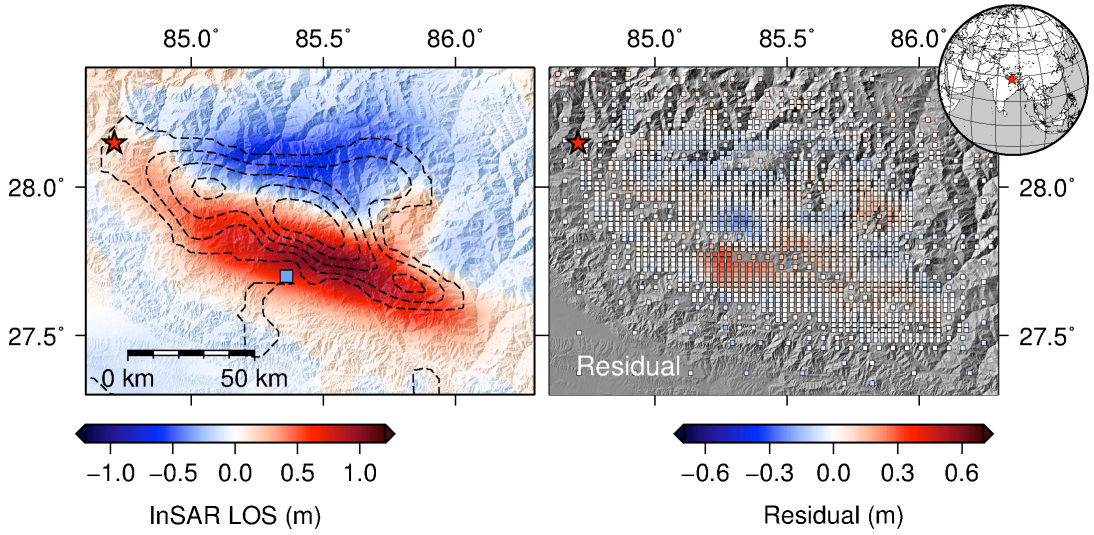

Fig. S1.

(A) Unwrapped line of sight (LOS) ground displacement maps measured from ALOS-2 satellite from repeat-pass interferometry between pre- and post-event SAR scenes (*18*), which give the motion of the Earth's surface along the line of sight of the satellite's radar. The dashed contours, are the 1 m slip contours from the final slip model. (B) Difference between observed and synthetic LOS displacements predicted from our best-fitting model. Warm colors indicate the model under-predicts surface displacements and cool colors indicate an over-prediction. The misfits suggest that the planar fault approximation is valid only to first order.

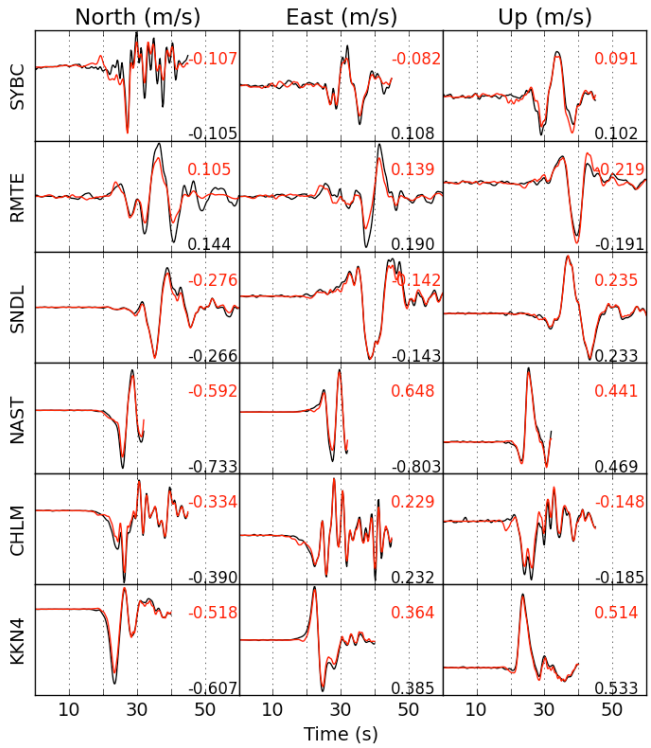

Fig. S2.

Comparison between the velocity waveforms derived from the 5 Hz GPS data (black) and the model predictions (red). Variance reduction is 74%. Peak displacement and velocity values are indicated next to each waveform.

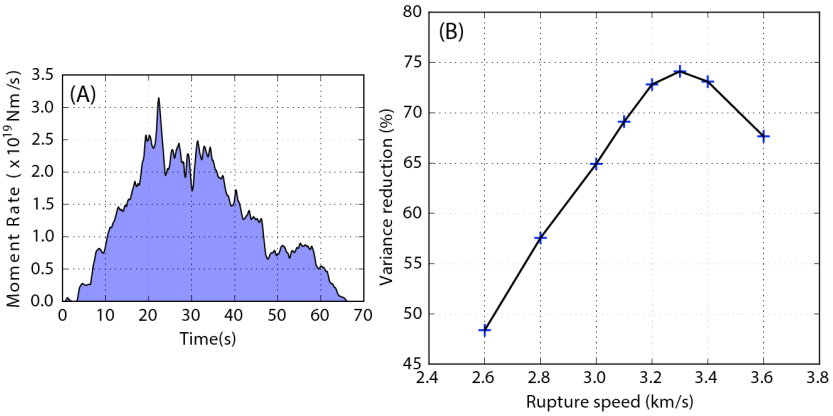

Fig. S3.

Kinematic source characteristics. (A) Moment release time function for the model in Figure 1C. (B) Variance reduction to the high-rate GPS waveforms as a function of maximum allowed rupture speed.

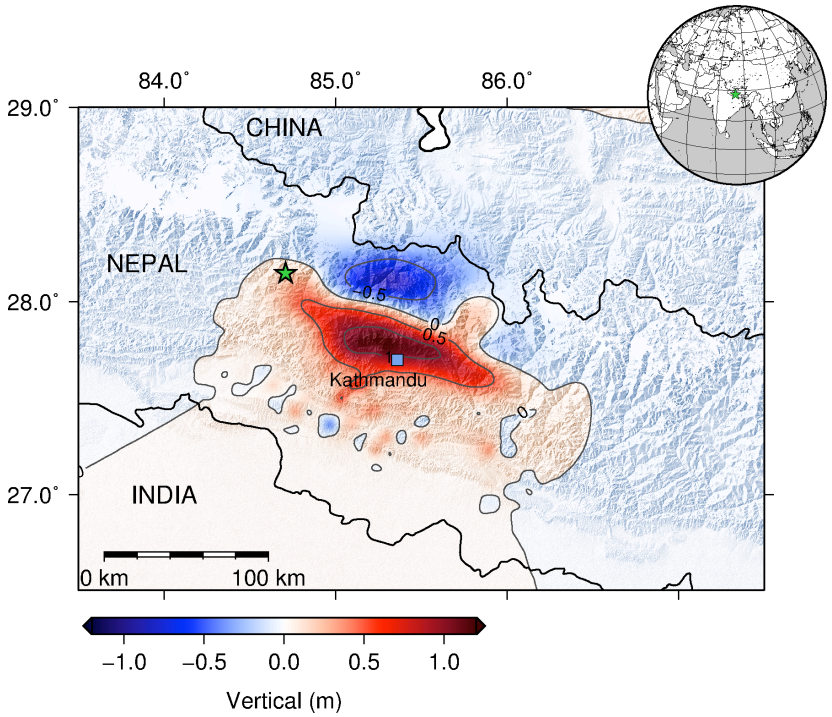

Fig. S4.

Vertical ground displacements due to the Gorkha earthquake. Vertical deformation predicted by the slip model of Figure 1A. Contours are every 0.5 m. The blue triangles are the locations of mountain peaks of the upper Himalayas with elevations above 7500 m.

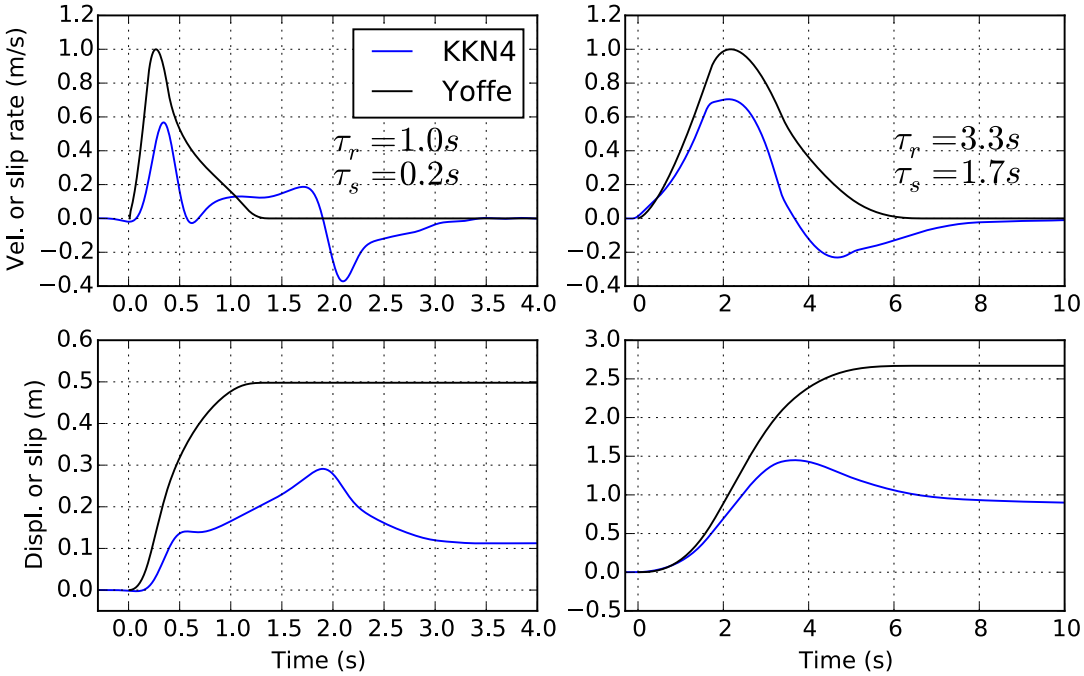

Fig. S5.

Synthetic tests comparing the imposed regularized Yoffe slip-rate time functions (STF) (Black line) with the displacement predicted at station KKN4. We considered two STFs with short and long onset times. The STF is somewhat smoothed after propagation from the source to station KKN4 through the layered media(*44*), but the smoothing can explain neither the long pulse duration observed in Figure 3 nor the smooth onset. These tests suggest that the surficial observation at the Kathmandu sites reflects well the STF on the fault. The amplitude of surface vertical displacement is about one third of the slip on the fault and the surface velocity is about 60% of the slip velocity.

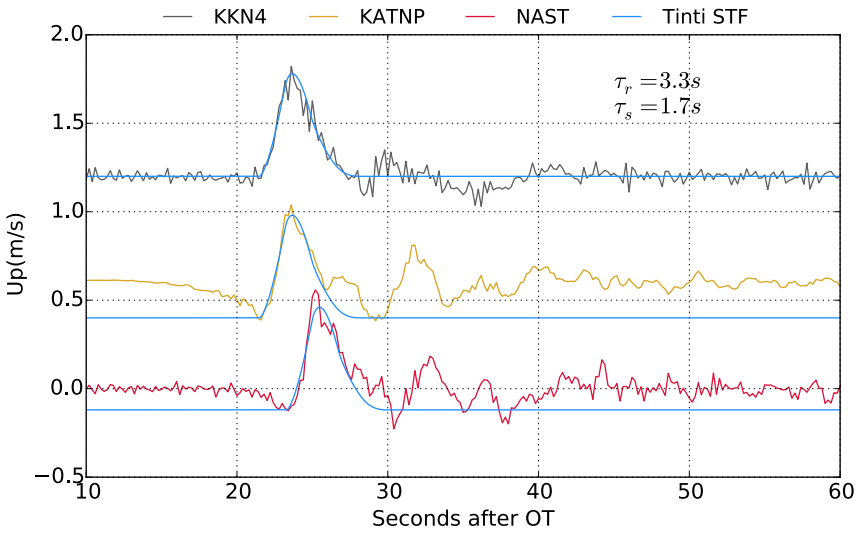

Fig. S6.

Regularized Yoffe slip-rate time function estimated from vertical velocity waveforms**.** Comparison between the vertical velocity waveforms observed at three sites around Kathmandu valley and the theoretical regularized Yoffe slip time function *(28)*.

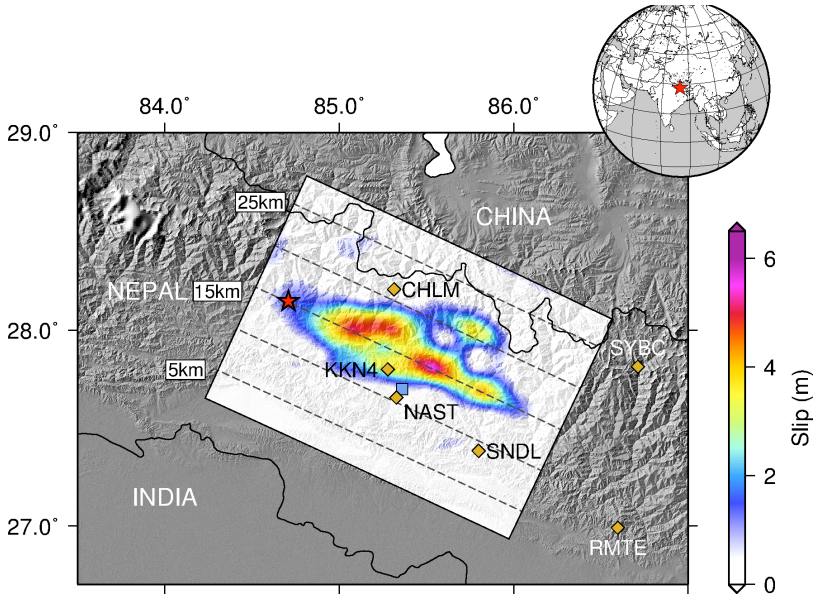

Fig. S7.

Static slip model from inversion of InSAR and GPS coseismic offsets. Orange diamonds are the locations of the 5 Hz GPS stations. Red star is mainshock epicenter. Blue square is Kathmandu.

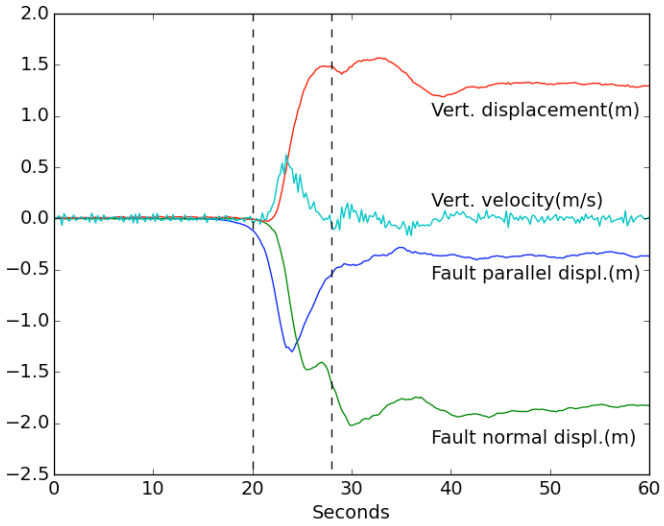

Fig. S8.

Fault parallel and fault perpendicular displacements at station KKN4 compared to the vertical velocity and displacement. The dashed lines are 7 s apart.

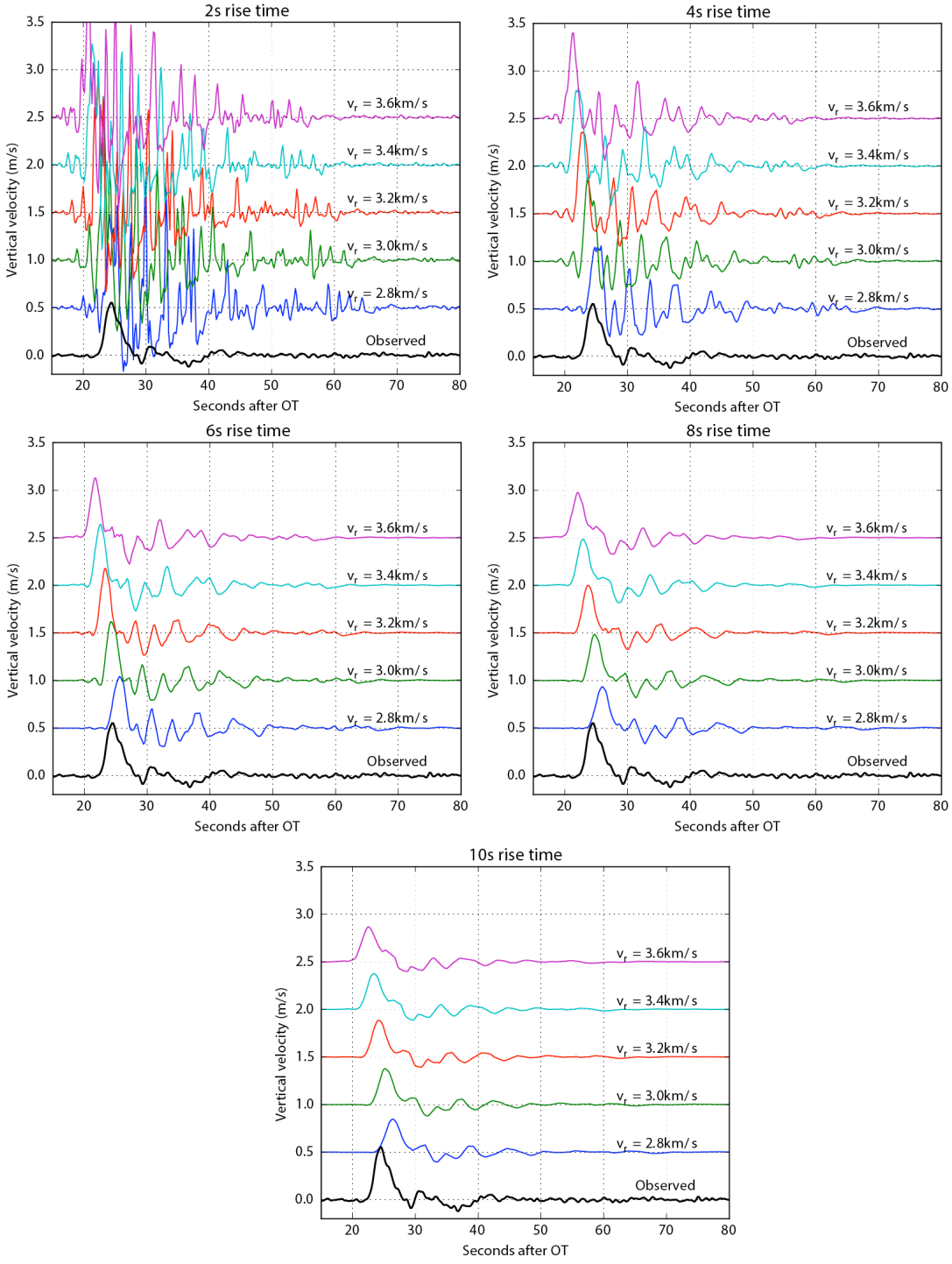

Fig. S9.

Synthetic vertical velocity waveforms at station KKN4 from the 25 scenario models compared to the recorded data (black trace). All models were computed using the static slip model of Figure S7.

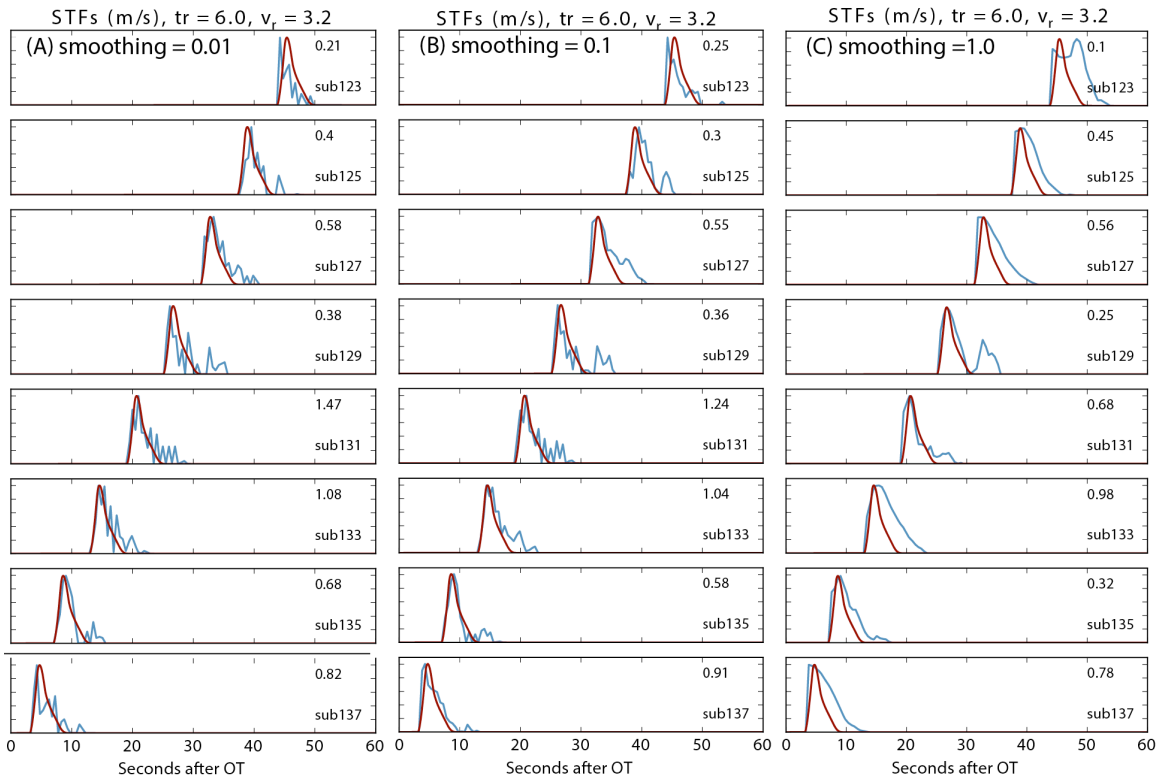

Fig. S10.

Source time functions for 9 subfaults on an along-strike profile. The brown lines are the regularized Yoffe STFs used in generating the synthetic model and the blue lines are the results of the inversion. The amplitude of each STF is indicated in each panel. This example is for a 6 s rise time propagating at 3.2 km. The inversion results are shown for 3 levels of temporal smoothing.

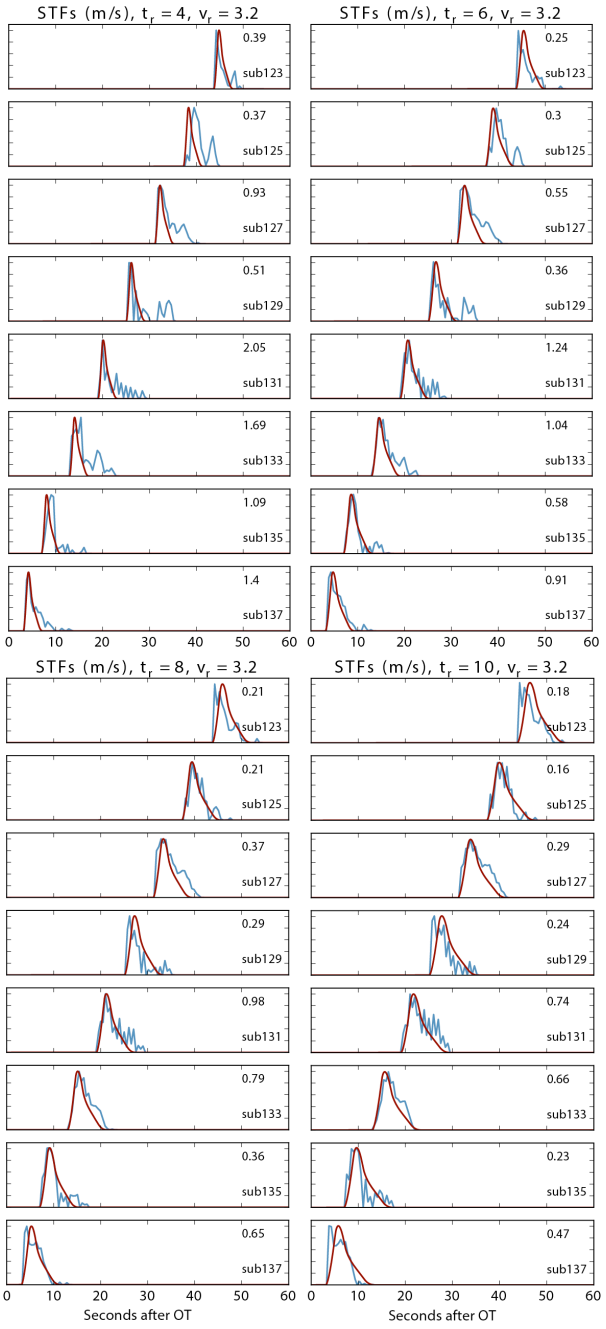

Fig. S11.

Source time functions for 9 subfaults on an along-strike profile. The brown lines are the regularized Yoffe STFs used in generating the synthetic models. The blue lines are the result of the inversion. All four models have the same rupture speed and are inverted with the same temporal smoothing value (0.1) the difference between them is the rise time used to generate the synthetic model.

Table S1.

Coordinates of GPS stations and coseismic offsets. Also indicated is the station's contribution to the inversion. The six GPS stations (in bold characters) were sampled at 5 Hz.

Station	Longitude	Latitude	East offset (m)	North offset (m)	Up offset (m)	Static offset used?	Vel. Waveform used?
KATNP	85.3157	27.7120	-	-	-	N/A	No
KKN4	85.2788	27.8008	-0.445 ±0.001	-1.830 ±0.002	1.260 ±0.003	Yes	Yes
NAST	85.3277	27.6567	-0.316 ±0.002	-1.300 ±0.002	0.606 ±0.007	Yes	Yes
SYBC	86.7124	27.8143	-0.004 ±0.006	-0.007 ±0.005	0.023 ±0.011	Yes	Yes
RMTE	86.5971	26.9910	0.007 ±0.003	0.000 ±0.003	-0.006 ±0.007	Yes	Yes
SNDL	85.7989	27.3849	0.047 ±0.002	-0.223 ±0.003	0.003 ±0.003	Yes	Yes
CHLM	85.3141	28.2073	-0.222 ±0.002	-1.390 ±0.003	-0.590 ±0.004	Yes	Yes
BELT	83.8257	27.4574	-0.007 ±0.007	0.004 ±0.004	0.004 ±0.018	Yes	N/A
BESI	84.3797	28.2286	-0.003 ±0.001	-0.002 ±0.001	-0.001 ±0.005	Yes	N/A
DMAU	84.2652	27.9734	-0.018 ±0.001	0.002 ±0.001	-0.001 ±0.005	Yes	N/A
GHER	84.4097	28.3746	0.019 ±0.002	-0.041 ±0.001	0.016 ±0.007	Yes	N/A
KIRT	85.2882	27.6819	-0.344 ±0.001	-1.475 ±0.001	0.736 ±0.007	Yes	N/A
DAMA	85.1077	27.6081	-0.215 ±0.002	-0.527 ±0.002	0.154 ±0.006	Yes	N/A

Table S2. Velocity model used for kinematic inversion *(45)*.

Vp (km/s)	Vs (km/s)	Density (kg/m^3)	Thickness (km)
5.50	3.20	2530	4.0
5.85	3.40	2640	12.0
6.00	3.50	2690	4.00
6.45	3.70	2830	6.50
6.65	3.85	2900	10.00
7.20	4.15	3070	5.00
7.50	4.20	3170	14.00
7.90	4.30	33000	-

Movie S1

Animation showing the propagation of the slip-rate pulse derived from the joint inversion of the high-rate GPS, static GPS and InSAR data, compared with the time-evolution of the sources of high frequency (05-2Hz) teleseismic waves (5). The cumulative slip distribution from the model is shown in Figure 1C. Each frame shows the instantaneous slip rate of the source model. The red star is the hypocenter and dashed lines represent the depth to the fault.